High interfacial-energy and lithiophilic Janus interphase enables stable lithium metal anodes

Guoxing Li, Shipeng Liu, Zhe Liu, Yingjie Zhao*

Prof. G. Li
Science Center for Material Creation and Energy Conversion, Institute of Frontier and Interdisciplinary Science, Shandong University, Qingdao, 266237, China.
E-mail: gxli@sdu.edu.cn

S. Liu, Prof. Y. Zhao
College of Polymer Science and Engineering, Qingdao University of Science and Technology, Qingdao 266042, China.

Dr. Z. Liu
Chemical Sciences and Engineering Division, Argonne National Laboratory, Lemont, IL 60439, USA.

Keywords: batteries, lithium metal anodes, solid electrolyte interphase, hybrid Janus interphase, interfacial energy

The stability of solid electrolyte interphase (SEI) layers is critical for developing lithium (Li) metal batteries. However, the fabrication of stable SEI layers is plagued by un-controlled structures, properties, and functions. Here we report a controllable design of an ordered LiF-rich and lithiophilic hybrid Janus interphase (LiF-HJI) using organic fluorination reagent as a functional SEI precursor. The LiF-HJI with a lower crystalline LiF layer and an upper Li organosulfide layer provides high interfacial energy with the Li metal and strong Li-ion affinity, allows homogenous Li-ion distribution, fast and uniform Li-ion transport, excellent mechanical and passivation properties, enabling stable Li metal anodes under harsh conditions, such as high deposition capacities (6 mA h cm^{-2}), current densities (10 mA cm^{-2}), and rates (5 C). Stable LiF-HJI@Li greatly improves cycling stability and capacity retention (80.1% after 300 cycles) of Li||LiNi$_{0.8}$Co$_{0.1}$Mn$_{0.1}$O$_2$ cells at a commercial-level areal capacity (~4.2 mA h cm^{-2}). Even under a lean-electrolyte condition of 3 g Ah^{-1}, 80% capacity retention can be maintained after 100 cycles, demonstrating excellent cycling performance under such harsh conditions.

1. Introduction

The rapid development of portable electronics and electric vehicles demands high-energy-density and high-power rechargeable batteries. Lithium (Li) metal batteries are the promising next-generation energy storage systems and being revived recently, due to the high theoretical specific capacity (3860 mA h g^{-1}) and low electrochemical potential (−3.04 V vs standard hydrogen electrode) of Li metal anodes.[1-5] However, the development of Li metal anodes is hindered by Li dendrite growth and low Coulombic efficiency (CE) of the Li plating/stripping which cause the safety hazards and short cycling life.[6-8] Therefore, resolving the fundamental challenges of the Li metal anodes is extremely urgent to enable the practical application of Li metal batteries.

The solid electrolyte interphase (SEI) layer plays a significant role in suppressing the Li dendrite growth and enhancing the Li plating/striping CE. SEI is a passivation layer derived from the electrolyte reduction on the anodes. Robust SEI layers can kinetically stabilize the anode/electrolyte interface and effectively prevent further consumption of the electrolyte, while also regulating Li-ion transport from the electrolyte onto the anode, and in turn, influencing the morphology of the Li deposition.[9-11] Although several emerging strategies are used to stabilize the Li metal anodes such as developing three dimensional (3D) porous Li hosts,[12-15] modifying current collectors,[16-21] and regulating Li-ion transport behavior,[8,22] the formed SEI layers in these strategies remain unstable owing to the lack of optimization of the SEI components and nanostructures. Engineering the SEI layers by optimizing electrolyte components can reinforce their stabilities,[3,23-28] but the SEI nanostructures, properties and functions can still not be accurately controlled. Typical SEI layers formed on the Li metal from standard carbonate/ether-based electrolytes consist of inorganic Li salts (LiF, Li_2O, Li_2CO_3, etc.) and organic components (RCOOLi, etc.)[29-33] which are distributed within the SEI heterogeneously, forming a mosaic nanostructure with both crystalline and amorphous properties (**Figure 1**a).

The low and nonuniform interfacial energy at SEI/Li, as well as the inferior flexibility and toughness of these SEI layers, lead to the failure to suppress the Li dendrite growth during Li plating/stripping process.[34] Moreover, in the mosaic SEI nanostructure, Li ions prefer to transporting at the crystalline/organic component interface,[35-39] the nonuniform distribution of nanocrystalline components in the SEI leads to the uneven Li-ion transport in the SEI, exacerbating the growth of Li dendrites.

Fabrication of artificial SEI layers[40-45] and Li protective layers[46-54] is attainable to regulate the SEI nanostructures and interface properties with high controllability and tunability. These artificial protective layers are typically made from organic or inorganic substances. SEI films prepared from the organic substances can accommodate the volume change during the Li plating/stripping process owing to the high flexibility, but show low interfacial energy with the Li metal, poor mechanical strength and Li-ion conductivity.[55-58] Artificial SEI layers composed of the inorganic substances (e. g., LiF, Li_3N, Li_2O) exhibit high SEI/Li interfacial energy, high mechanical hardness and Li-ion conductivity,[59-63] as well as uniform Li-ion transport enabled by the even distribution of inorganic crystalline grains in the inorganic SEI layers, benefiting the uniform Li deposition.[38] However, these inorganic layers prone to break after continuous plating/stripping process and lose the long-term and effective protection of the Li metal anodes owing to their rigid and brittle nature (Figure 1b). Therefore, the rational design of the SEI layers with controlled structures, properties, and functions is desirable. An ideal SEI layer should have an ordered nanostructure with an effective combination of multifunctional organic and inorganic layers to enable high SEI/Li interfacial energy, fast and uniform Li-ion transport, as well as excellent mechanical properties, which are essential to achieve stable Li metal anodes (Figure 1c).

Herein, we develop an ordered LiF-rich and lithiophilic hybrid Janus interphase (LiF-HJI) to stabilize the Li metal anodes. The LiF-HJI is obtained via a controllable growth of lower crystalline LiF layer and upper Li bis(2-methoxyethyl) aminosulfide (Li-MAS) organic layer successively by simply soaking the Li metal in the bis(2-methoxyethyl) aminosulfur trifluoride (Deoxo-Fluor, designated as D-F) solution. The attractive properties of LiF and Li-MAS as well as the ordered and layered structures endow the LiF-HJI with unique features. The compact crystalline LiF layer with the uniform distribution of crystalline grains provides not only necessary mechanical hardness and high interfacial energy with the Li metal, but also fast and uniform Li-ion transport through the LiF grain boundaries. The Li-MAS layer, containing PEO-like organic chain, effectively facilitates the Li-ion transfer, and the polar functional groups (C-N, C-O, N-S) in the Li-MAS layer have strong Li-ion affinity and guide the uniform distribution of the Li ions. Meanwhile, this organic layer enhances the flexibility of the LiF-HJI and functions as a "stress-release" layer to prevent the cracking of the underneath LiF layer during the Li plating/stripping process. Therefore, under the protection of the multifunctional LiF-HJI, the stability of Li metals in humid air (~50% relative humidity) is significantly improved, and the Li metal anodes exhibit excellent cycling stability under harsh conditions without Li dendrite growth, such as high current densities (e. g., 10 mA cm^{-2}), high deposition capacities (e. g., 6 mA h cm^{-2}), and high rates (e. g., 5 C). Full cells containing LiF-HJI protected Li metal (LiF-HJI@Li) anodes and commercial-level areal capacity $LiNi_{0.8}Co_{0.1}Mn_{0.1}O_2$ (NCM811, ~4.2 mA h cm^{-2}) cathodes show excellent cycling stability and capacity retention (80.1% after 300 cycles) with an average CE of 99.67%. Even under lean-electrolyte conditions (e. g., 3 g Ah^{-1}), the full cells still exhibit stable cycling over 200 cycles with a remarkably improved capacity retention.

2. Results and Discussion

2.1. Preparation and characterization of LiF-HJI@Li.

The LiF-HJI@Li was prepared by soaking the Li metal into the D-F solution for 48 h. D-F was selected as the reactive agent to fabricate the stable interphase considering it contains a PEO-like chain and strong fluorination group of $-SF_3$, which could provide multifunctional organic and inorganic components to endow the interphase with unique properties. D-F can react with Li metal to form LiF and Li-MAS successively, the inorganic LiF layer was firstly formed on the Li metal surface, followed by covering a Li-MAS layer to form an organic/inorganic hybrid Janus interphase (**Figure 2**a). Chemical characterization of the LiF-HJI@Li was conducted using Fourier transform infrared (FT-IR) spectroscopy, X-ray diffraction (XRD), and X-ray photoelectron spectroscopy (XPS) techniques. FT-IR spectrum of the LiF-HJI@Li (Figure 2b) shows two peaks at ~1458 cm^{-1} and ~638 cm^{-1}, which are attributed to the standard vibration peaks of pure LiF, indicating the presence of LiF in the LiF-HJI. The existence of LiF can be further proved by the XRD pattern, the peak at 45° is indexed as LiF (PDF# 00-004-0857), confirming the crystalline nature of the LiF layer (Figure 2c). Other strong peaks around 1271 cm^{-1}, 1113 cm^{-1}, and 777 cm^{-1} in FT-IR spectrum of the LiF-HJI@Li (Figure 2b) are attributed to the vibrations of C-N, C-O, and N-S bonds of Li-MSA, respectively. The peaks corresponding to C-N and N-S bonds shift to high wavenumbers compared with those of D-F, owing to a change in the chemical environment induced by the replacement of -SF_3 group by -SLi after the reaction of D-F with the Li metal, which can be further confirmed by the disappearance of S-F vibration peak around 826 cm^{-1} in FT-IR spectrum of the LiF-HJI@Li. XPS spectra show the presence of C, S, F, N, and O elements in the LiF-HJI (Figure S1), the S, F, and N elements originate from the reaction products of D-F. Evidenced from S 2p XPS spectrum of the LiF-HJI@Li (Figure 2d), the strong peak at 163.3 eV corresponds to the S $2p_{3/2}$ for Li organosulfide, confirming Li-MAS exists in the LiF-HJI. The F 1s XPS spectrum shows a peak at 685.1 eV, which is assigned to the F 1s from LiF (Figure 2e). Combined all the results of FT-IR, XRD, and XPS, we can conclude that the LiF-HJI is composed of crystalline inorganic LiF and organic Li-MAS deriving from the reaction between D-F and the Li metal.

Scanning electron microscopy (SEM) and transmission electron microscopy (TEM) were used to investigate the morphology of the LiF-HJI@Li. As shown in the inset of Figure 2f, the pretreated Li metal remains shiny after the LiF-HJI coating. The top-view SEM images show the Li metal surface is uniformly covered by the LiF-HJI with a relatively smooth surface (Figure 2f-g). The corresponding elemental mapping results (Figure S2) reveal the uniform distribution of LiF and Li-MAS. The cross-section SEM images display a continuous coating of the LiF-HJI covering the Li metal with a lower LiF layer and an upper Li-MAS layer (Figure 2h, Figure S3). The thickness of the LiF-HJI is around 540 nm (the thicknesses of the LiF layer and Li-MAS layer are around 450 nm and 90 nm, respectively), and the wrinkles observed in the free-standing LiF-HJI reflect its good flexibility (Figure 2i). The TEM image clearly shows the amorphous organic layer tightly covers on the LiF layer (Figure 2j), and this Janus layer is ordered and uniform, confirmed by the TEM elemental mapping images (Figure S4) which illustrate the homogenous distribution of F, C, S and N atoms, consistent with the SEM elemental mapping results. The selected area electron diffraction (SEAD) pattern (inset in Figure 2k) further reveals the crystalline structure of LiF, the high-resolution TEM image (Figure 2k) demonstrates the (111) lattice plane of LiF with a plane spacing of 0.232 nm.

2.2. Dynamic formation process of LiF-HJI@Li.

To elucidate the dynamic formation process of the LiF-HJI@Li, its morphology evolution and corresponding chemical compositions at various soaking times were investigated. In the beginning, only LiF particles were formed on the Li metal as shown in the SEM image (**Figure 3**a), evidenced by the strong signal of element F with a content of ~90% in the corresponding energy dispersive spectroscopy (EDS) of SEM (Figure S5a, Table S1). Along with the soaking time increasing, more and more LiF particles were produced and accumulated together to form a dense LiF layer (Figure 3b). Subsequently, the Li-MAS layer began to grow along the surface of the LiF layer and could be distinguished in the dark areas (Figure 3c-d), further proved by the appearance of S and N signals in the SEM-EDS result (Figure S5b). The Li-MAS layer kept growing (Figure 3e), confirmed by the increasing intensities and contents of S and N as well as the relatively dropping of F content (Figure S5c-d, Table S1), and completely covered all the LiF layer at the soaking time of 48 h to form the LiF-HJI (Figure 3f), which has a hybrid Janus structure with an upper organic layer and a lower inorganic layer exhibiting different properties and functions (Figure S3). Further extending the soaking time, the surface of the film became much rougher (Figure S6), probably because of the nonuniform deposition of the organic component when its concentration in the solution became low. Despite the morphologies of the artificial layers after 48 h became slightly different, the contents of the F, S, N, and C elements in the artificial layer were relatively stable (Table S1, Figure S5d-f), suggesting the similar compositions in the LiF-HJI. Therefore, the results of the morphology-evolution investigation reflect the growth of LiF-HJI is ordered and controllable, we can tune the soaking time to get different morphologies and chemical compositions of the artificial layers. To ensure the formation of a relatively smooth and homogeneous LiF-HJI, the soaking time was held for 48 h in this work.

FT-IR and XPS were conducted to further analyze the chemical compositions of the interphase at various soaking times. Consistent with the morphology evolution and SEM-EDS results, the FT-IR spectra only show gradually increased LiF peak in the beginning (Figure 3g, Figure S7), then the vibration peaks of C-N, C-O, and N-S bonds from the organic Li-MAS layer (Figure 3g) appear and become stronger with increasing the soaking time, and maintain stable after 48 h (Figure S8). A similar trend could also be found in the XPS spectra which show the high intensity of LiF at first (Figure 3h), then the signals of S and N are detected (Figure 3i-j, Figure S9). These FT-IR and XPS results consolidate that only LiF was yielded at the beginning of the soaking process to form the inorganic LiF layer, then the Li-MAS layer started to grow on the top of the LiF layer to get the inorganic/organic hybrid Janus layer.

2.3. Growth mechanism of LiF-HJI@Li.

Based on the results of the morphology-evolution investigation and chemical-composition analysis, we could hypothesize a mechanism for the LiF-HJI@Li growth. As shown in **Figure 4**a, the fluorination group -SF_3 of D-F reacts with the Li metal to generate a possible intermediate -SF and the final product -SLi, which is accompanied by the formation of LiF during the entire redox process (Figure S10). In the beginning, the conversion of fluorination groups from -SF_3 to -SF dominates the reaction owing to a relatively high concentration of D-F near the Li metal surface, meanwhile most of the LiF is generated on the Li metal surface to form an inorganic layer in this step. With the continuous consumption of D-F and increase of -SF concentration, -SF group will be further reduced to -SLi, and the formed LiF at this step, despite a relatively small amount, will further thicken the LiF layer. The final reduction product of Li organosulfide (Li-MAS), which probably has a lower solubility than the fluorination reagent in hexane due to the increased polar, will cover the LiF film to form an organic layer when its concentration continuously increases. At last, the hybrid Janus layer with lower LiF and upper Li-MAS is fabricated. The prepared LiF-HJI can significantly improve the stability of the Li metal in humid air (~50% relative humidity) (Figure 4b), indicating its effective protection and passivation for the Li metal. The excellent stability of the LiF-HJI@Li in the air also suggests its potential compatibility with industrial electrode fabrication processes.

The attractive features of LiF and Li-MAS, as well as the ordered LiF/Li-MAS hybrid structure endow the LiF-HJI with unique and multifunctional properties. Firstly, the high interfacial energy of LiF with the Li metal facilitates the deposited Li to laterally grow along the LiF-HJI/Li interface and prevents it from penetrating the protective layer.[34,59,61] Meanwhile, homogenous crystalline LiF grains in the compact LiF layer can enable a fast and uniform Li-ion transport through the grain boundaries.[38,64] Together with the high mechanical hardness, the LiF layer is favorable for suppressing dendrite growth and enabling uniform Li deposition. Secondly, the Li-MAS layer, which is a kind of Li organosulfide and contains PEO-like organic chain, could promote the Li-ion transport. Moreover, the polar functional groups (C-N, C-O, N-S) in the Li-MAS layer have strong Li-ion affinity and can guide the uniform distribution of the Li ions.[12,19,65] Additionally, this organic layer of the Li organosulfide can enhance the flexibility of the LiF-HJI,[3,24] and serve as a "stress-release" layer to prevent the cracking of the lower LiF layer during Li plating/stripping process. The mechanical properties of Li-HJI@Li can be investigate by Atomic force microscopy (AFM).[66] As a comparison, LiF@Li was also prepared by soaking the Li metal in D-F solution for 6 h. As shown in Figure S11, the Young's modulus of LiF-HJI@Li is around 391.9 MPa (Figure S11a), which is lower than that of LiF@Li (1.499 GPa) (Figure S11b), due to the coverage of the organic Li-MAS layer. The surface of Li-HJI@Li shows a larger deformation and hysteresis between the approach and withdrawal curves, along with a long pull-off before the tip completely returned to the free-standing position. All these results suggest that the LiF-HJI@Li is flexible, indicating a good mechanical property of the LiF-HJI. Thirdly, pure organic layer usually has strong bonding (low interfacial energy) with the Li metal, causing the SEI to suffer the same volume change as Li during Li plating/stripping,[55,56] the ordered LiF/Li-MAS hybrid structure provides an intermediate LiF layer to avoid direct contact between the organic layer and the Li metal, thereby eliminating the aforementioned issue while preserving the benefits of the organic layer. Overall, the LiF-HJI combines the unique properties of both high interfacial energy and Li-ion affinity originating from the inorganic and organic species, respectively, and enables even Li-ion distribution, uniform and fast Li-ion transport, as well as enhanced mechanical properties, which are beneficial for the dendrite-free Li deposition and improvement of CE (Figure 4c). By contrast, in the traditional mosaic SEI layers, the random distribution of inorganic and organic substances could not effectively regulate the Li-ion distribution and transport in the SEI at the nanoscale level. Li ions prefer to transferring at the crystalline/organic component interface,[35-39] leading to the nonuniform Li-ion transport and Li deposition (Figure 4c). Moreover, the difference in the interfacial energy of organic and inorganic species with the Li metal will lead to a different deformation stress in the SEI layer, exacerbating the cracking of the SEI layers.

2.4. Electrochemical performance of LiF-HJI@Li anodes.

The unique and multifunctional properties of the LiF-HJI significantly improve the electrochemical performance of Li metal anodes. Symmetric Li metal cells with carbonate electrolyte were assembled to evaluate the stability of the Li metal anodes. At a current density of 2 mA cm^{-2} and a deposition capacity of 2 mA h cm^{-2} (**Figure 5**a), the LiF-HJI@Li anodes deliver good cycling stability with a low overpotential around 50 mV for over 480 h. Whereas, the bare Li metal anodes exhibit a sudden increase in hysteresis after 200 cycles, attributing to the irregular Li plating/stripping and severe breaking/repairing of the SEI layer. The nucleation overpotential (μ_n) and plateau overpotential (μ_p) are related to the energy barrier of Li nucleation process and mass-transfer process, respectively,[67,68] which could reflect the fundamental nucleation behavior of Li ions under different SEI layers during plating process. As shown in Figure S12, the LiF-HJI@Li anodes show much lower μ_n (0.0235 V) and μ_p (0.0645 V) than those of bare Li metal anodes (μ_n = 0.0465 V; μ_p = 0.0766 V), indicating the reduced energy barrier of Li nucleation and growth enabled by the LiF-HJI which can provide high interfacial energy with the Li metal and fast Li-ion transport. Under the conditions of high current densities and deposition capacities (4 mA cm^{-2} and 4 mA h cm^{-2}; 6 mA cm^{-2} and 6 mA h cm^{-2}), the LiF-HJI@Li anodes still display stable and steady overpotential profiles for 200 h (Figure 5b) and 100 h (Figure 5c), respectively. In sharp contrast, the bare Li metal anodes encounter large overpotentials and fluctuated voltage profiles and fail after several dozens of cycles. The striking difference in cycling stability between these two kinds of anodes indicates the LiF-HJI is robust enough to extend the cycling life at various current densities and deposition capacities. Moreover, the LiF-HJI@Li anodes display lower overpotentials than those of bare Li metal anodes at all the testing conditions (Figure S13), further indicating the fast Li-ion transport through the electrolyte/electrode interphase enabled by the unique LiF-HJI. It is noted that the higher initial voltage polarization of the LiF-HJI@Li than that of the bare Li metals is probably attributed to the tight coverage of the protective layer on the Li metal before cycling. When a high rate of 5 C (a current density of 10 mA cm^{-2} and a deposition capacity of 2 mA h cm^{-2}) was applied, the LiF-HJI@Li anodes still deliver stable cycling over 90 h with a relatively low overpotential (Figure S14), showing the promise for the application in fast-charging Li metal batteries. To better understand the electrochemical stability, the morphology of the LiF-HJI@Li anodes after cycling was further investigated. As shown in the SEM images (Figure 5d-g), the dendrite-free, uniform, and compact Li deposition is achieved, the LiF-HJI still covers the Li metal surface tightly and maintains its structure without obvious cracks after cycling. The cycling stability and morphology of the Li metal anodes only protected by crystalline LiF layer (LiF@Li) were also investigated, which could, on the other hand, reveal the necessity of the organic layer. The LiF@Li was obtained by soaking the Li metal in D-F solution for 6 h. The symmetric LiF@Li cells show a stable cycling for over 300 h (Figure S15), which is better than bare Li metal anodes, but the following increased hysteresis indicates its inferior performance to the LiF-HJI@Li anodes, attributing to the lack of upper organic layer to prevent the cracking of the rigid LiF layer after long-cycle Li plating/stripping, which could be further confirmed by the SEM morphologies demonstrating a lot of cracks in the LiF layer after cycling (Figure S16). The electrochemical properties of the LiF-HJI@Li anodes after exposing in the humid air (~50% relative humidity) for 4 h was also investigated. As shown in Figure S17, the LiF-HJI@Li symmetric cells still deliver a relatively stable cycling for 250 h at a current density of 2 mA cm^{-2} and a deposition capacity of 2 mA h cm^{-2}, suggesting the effective protection for the Li metal against the humid air. Combining the above electrochemical measurements and SEM morphologies, it is reasonable to ascribe the excellent cycling performance of LiF-HJI@Li anodes to the stable LiF-HJI which provides high interfacial energy with the Li metal, uniform and fast Li-ion transport, as well as the good mechanical properties to enable the dendrite-free Li deposition.

Phase-field simulation of Li deposition was performed to theoretically validate and explicate the role of the LiF-HJI in maintaining stable Li metal anodes. Consistent with the experimentally observed morphology, the simulated morphology shows compact and dendrite-free Li deposition under the protection of the LiF-HJI (Figure 5h, Figure S18a-e). The LiF-HJI enables the homogenous distributions of the Li-ion concentration, Li-ion flux and Li-ion concentration gradient (Figure 5i-j), contrast sharply with the traditional mosaic SEI covered Li metals which show the dendritic Li deposition with inhomogenous Li-ion concentration distribution, nonuniform Li-ion flux and Li-ion concentration gradient (Figure 5k-m, Figure S18f-j). These simulation results confirm that the lower LiF layer of the LiF-HJI possessing a high interfacial energy with the Li metal can effectively confine the spatial freedom of Li nucleation (Figure S18a-e); and the upper Li-ion-affinity Li-MAS layer, together with the homogenous crystalline LiF grains in the LiF layer, can enable a fast and uniform Li-ion diffusion; all of which result in a uniform Li deposition.

The stable LiF-HJI@Li anodes greatly improve the full-cell performance of Li metal batteries. Full cells (LiF-HJI@Li||NCM811) containing LiF-HJI@Li anodes and high-areal-capacity NCM811 (~4.2 mA h cm^{-2}) cathodes were assembled. The amount of the electrolyte used in the full cells notably influences the energy density of the Li metal batteries. A limited amount of the electrolyte (lean electrolyte) used in the cells is the prerequisite for their practical application. Therefore, the cycling performance of the cells using various amounts of the electrolyte were also evaluated in this work. Under a flooded-electrolyte condition (**Figure 6**a), the cells with LiF-HJI@Li deliver a high initial discharge capacity of 164.5 mA h g^{-1}, and maintain the capacity of 131.7 mA h g^{-1} after 300 cycles (80.1% capacity retention) with an average CE of 99.67%, showing an excellent cycling performance (Table S2). While the control cells display a quick CE drop and fast capacity decay after 80 cycles, ascribing to the failure of the Li metal anodes at such a high deposition capacity. The charge/discharge profiles show a smaller polarization of the cells with LiF-HJI@Li than that of the control cells (Figure 6b-c,

Figure S19), further demonstrating the faster Li-ion transport in LiF-HJI than the traditional SEI layer. The cycling performance of the Li metal batteries under lean-electrolyte conditions could better reflect the stability of the Li metal anodes, because the unstable Li metals lead to a serious consumption of the electrolyte and significantly decrease the cycling life.[25,69] When the lean-electrolyte conditions of 6 g Ah^{-1} (Figure 6d) and 3 g Ah^{-1} (Figure 6e) were used, respectively, the cells with LiF-HJI@Li anodes can still run over 200 cycles with greatly improved capacity retention and CE, showing superior performance over the control cells. In particular, 80% capacity retention can be maintained after 100 cycles for the cells under the lean-electrolyte condition of 3 g Ah^{-1}, showing a peerless cycling performance under such harsh conditions (Table S2), which further demonstrates that the LiF-HJI provides effective passivation for the Li metal anodes and remarkably reduce the consumption of the electrolyte.

3. Conclusion

In summary, we have demonstrated a strategy to fabricate an ordered high interfacial-energy and lithiophilic hybrid Janus interphase to stabilize the Li metal anodes. Unlike the traditional mosaic SEI layers and common single-component artificial interphase layers, the LiF-HJI combines the attractive properties of the homogenous and ordered crystalline LiF and Li-MAS layers to intrinsically improve the interfacial energy with the Li metal, regulate Li-ion distribution, accelerate Li-ion transport, and optimize the mechanical properties to enable dendrite-free Li deposition and improved CE under harsh conditions, such as high deposition capacities (e. g., 6 mA h cm^{-2}), high current densities (e. g., 10 mA cm^{-2}), and high rates (e. g., 5 C). Meanwhile, the LiF-HJI coated Li metals exhibit high corrosion resistance to the humid air (~50% relative humidity), showing the promise in practical industry in the future. Thanks to the unique features of the LiF-HJI@Li, the LiF-HJI@Li||NCM811 full cells with commercial-level areal capacity exhibit excellent cycling stability and capacity retention, as well as significantly enhanced CE, even under lean-electrolyte conditions (e. g., 3 g Ah^{-1}), demonstrating the great potential for next-generation high-performance Li metal batteries. The strategy not only contributes significantly to the Li metal batteries, but could also be applicable in other fields facing unstable interface issues, such as Si anodes, high-nickel cathodes and solid-state electrolytes.

Supporting Information

Supporting Information is available from the Wiley Online Library or from the author.

Acknowledgements

This work was supported by the National Natural Science Foundation of China (52072222), the Qilu Youth Scholar Funding of Shandong University (62460082063114), and the Taishan Scholar Project of Shandong Province of China (62460082061017). G. L. acknowledges financial support from Thousand Youth Talents Plan of China. Simulation work was supported by the U.S. Department of Energy, Office of Energy Efficiency and Renewable Energy, Vehicle Technologies Office under contract DE-AC02-06CH11357. The authors appreciate Dr. Shabbir Ahmed at Argonne National Laboratory and Prof. Yuliang Li at Institute of Chemistry, Chinese Academy of Sciences for the discussion on the manuscript.

Received: ((will be filled in by the editorial staff))
Revised: ((will be filled in by the editorial staff))
Published online: ((will be filled in by the editorial staff))

References

[1] M. S. Whittingham, *Science* **1976**, *192*, 1126.

[2] H. Kim, G. Jeong, Y.-U. Kim, J.-H. Kim, C.-M. Park, H.-J. Sohn, *Chem. Soc. Rev.* **2013**, *42*, 9011.

[3] G. Li, Y. Gao, X. He, Q. Huang, S. Chen, S. H. Kim, D. Wang, *Nat. Commun.* **2017**, *8*, 850.

[4] A. Zhamu, G. Chen, C. Liu, D. Neff, Q. Fang, Z. Yu, W. Xiong, Y. Wang, X. Wang, B. Z. Jang, *Energy Environ. Sci.* **2012**, *5*, 5701.

[5] G. Li, Adv. *Energy Mater*. **2021**, *11*, 2002891.

[6] J. M. Tarascon, M. Armand, *Nature* **2001**, *414*, 359.

[7] W. Xu, J. Wang, F. Ding, X. Chen, E. Nasybulin, Y. Zhang, J.-G. Zhang, *Energy Environ. Sci.* **2014**, *7*, 513.

[8] G. Li, Z. Liu, Q. Huang, Y. Gao, M. Regula, D. Wang, L.-Q. Chen, D. Wang, *Nat. Energy* **2018**, *3*, 1076.

[9] W. Huang, H. Wang, D. T. Boyle, Y. Li, Y. Cui, *ACS Energy Lett*. **2020**, *5*, 1128.

[10] E. Peled, S. Menkin, *J. Electrochem. Soc*. **2017**, *164*, A1703.

[11] M. B. Pinson, M. Z. Bazant, *J. Electrochem. Soc*. **2013**, *160*, A243.

[12] Z. Liang, G. Zheng, C. Liu, N. Liu, W. Li, K. Yan, H. Yao, P.-C. Hsu, S. Chu, Y. Cui, *Nano Lett*. **2015**, *15*, 2910.

[13] D. Lin, Y. Liu, Z. Liang, H.-W. Lee, J. Sun, H. Wang, K. Yan, J. Xie, Y. Cui, *Nat. Nanotechnol*. **2016**, *11*, 626.

[14] Y. Liu, D. Lin, Z. Liang, J. Zhao, K. Yan, Y. Cui, *Nat. Commun*. **2016**, *7*, 10992.

[15] H. Ye, S. Xin, Y.-X. Yin, J.-Y. Li, Y.-G. Guo, L.-J. Wan, *J. Am. Chem. Soc*. **2017**, *139*, 5916.

[16] C.-P. Yang, Y.-X. Yin, S.-F. Zhang, N.-W. Li, Y.-G. Guo, *Nat. Commun.* **2015**, *6*, 8058.

[17] Q. Yun, Y.-B. He, W. Lv, Y. Zhao, B. Li, F. Kang, Q.-H. Yang, *Adv. Mater*. **2016**, *28*, 6932.

[18] T.-T. Zuo, X.-W. Wu, C.-P. Yang, Y.-X. Yin, H. Ye, N.-W. Li, Y.-G. Guo, *Adv. Mater.* **2017**, *29*, 1700389.

[19] L. Fan, H. L. Zhuang, W. Zhang, Y. Fu, Z. Liao, Y. Lu, *Adv. Energy Mater*. **2018**, *8*, 1703360.

[20] H. Shang, Z. Zuo, Y. Li, *ACS Appl. Mater. Interfaces* **2019**, *11*, 17678.

[21] Z. Zuo, F. He, F. Wang, L. Li, Y. Li, *Adv. Mater.* **2020**, *32*, 2004379.

[22] G. Li, Z. Liu, D. Wang, X. He, S. Liu, Y. Gao, A. AlZahrani, S. H. Kim, L. Q. Chen, D. Wang, *Adv. Energy Mater*. **2019**, *9*, 1900704.

[23] X. Fan, L. Chen, O. Borodin, X. Ji, J. Chen, S. Hou, T. Deng, J. Zheng, C. Yang, S.-C. Liou, K. Amine, K. Xu, C. Wang, *Nat. Nanotechnol*. **2018**, *13*, 715.

[24] G. Li, Q. Huang, X. He, Y. Gao, D. Wang, S. H. Kim, D. Wang, *ACS Nano* **2018**, *12*, 1500.

[25] J. Qian, W. A. Henderson, W. Xu, P. Bhattacharya, M. Engelhard, O. Borodin, J.-G. Zhang, *Nat. Commun*. **2015**, *6*, 6362.

[26] C. Yan, Y.-X. Yao, X. Chen, X.-B. Cheng, X.-Q. Zhang, J.-Q. Huang, Q. Zhang, *Angew. Chem. Int. Ed*. **2018**, *57*, 14055.

[27] X. Q. Zhang, T. Li, B. Q. Li, R. Zhang, P. Shi, C. Yan, J. Q. Huang, Q. Zhang, *Angew. Chem. Int. Ed*. **2020**, *59*, 3252.

[28] J. Zheng, M. H. Engelhard, D. Mei, S. Jiao, B. J. Polzin, J.-G. Zhang, W. Xu, *Nat. Energy* **2017**, *2*, 17012.

[29] D. Aurbach, B. Markovsky, A. Shechter, Y. Ein‐Eli, H. Cohen, *J. Electrochem. Soc*. **1996**, *143*, 3809.

[30] D. Aurbach, A. Zaban, Y. Gofer, Y. E. Ely, I. Weissman, O. Chusid, O. Abramson, *J. Power Sources* **1995**, *54*, 76.

[31] D. Aurbach, E. Zinigrad, Y. Cohen, H. Teller, *Solid State Ion.* **2002**, *148*, 405.

[32] E. Peled, *J. Power Sources* **1983**, *9*, 253.

[33] C. Yan, X.-B. Cheng, C.-Z. Zhao, J.-Q. Huang, S.-T. Yang, Q. Zhang, *J. Power Sources* **2016**, *327*, 212.

[34] S. Liu, X. Ji, J. Yue, S. Hou, P. Wang, C. Cui, J. Chen, B. Shao, J. Li, F. Han, J. Tu, C. Wang, *J. Am. Chem. Soc.* **2020**, *142*, 2438.

[35] A. C. Balazs, T. Emrick, T. P. Russell, *Science* **2006**, *314*, 1107.

[36] F. Croce, G. B. Appetecchi, L. Persi, B. Scrosati, *Nature* **1998**, *394*, 456.

[37] J. Janek, W. G. Zeier, *Nat. Energy* **2016**, *1*, 16141.

[38] Y. Li, W. Huang, Y. Li, A. Pei, D. T. Boyle, Y. Cui, *Joule* **2018**, *2*, 2167.

[39] W. Liu, S. W. Lee, D. Lin, F. Shi, S. Wang, A. D. Sendek, Y. Cui, *Nat. Energy* **2017**, *2*, 17035.

[40] M. S. Kim, J.-H. Ryu, Deepika, Y. R. Lim, I. W. Nah, K.-R. Lee, L. A. Archer, W. Il Cho, *Nat. Energy* **2018**, *3*, 889.

[41] N.-W. Li, Y. Shi, Y.-X. Yin, X.-X. Zeng, J.-Y. Li, C.-J. Li, L.-J. Wan, R. Wen, Y.-G. Guo, *Angew. Chem. Int. Ed*. **2018**, *57*, 1505.

[42] N.-W. Li, Y.-X. Yin, C.-P. Yang, Y.-G. Guo, *Adv. Mater*. **2016**, *28*, 1853.

[43] Y. Liu, D. Lin, P. Y. Yuen, K. Liu, J. Xie, R. H. Dauskardt, Y. Cui, *Adv. Mater*. **2017**, *29*, 1605531.

[44] Q. Yang, M. Cui, J. Hu, F. Chu, Y. Zheng, J. Liu, C. Li, *ACS Nano* **2020**, *14*, 1866.

[45] Y. Zhou, X. Zhang, Y. Ding, L. Zhang, G. Yu, *Adv. Mater.* **2020**, *32*, 2005763.

[46] D. Lee, S. Sun, J. Kwon, H. Park, M. Jang, E. Park, B. Son, Y. Jung, T. Song, U. Paik, *Adv. Mater*. **2020**, *32*, 1905573.

[47] X. Liang, Q. Pang, I. R. Kochetkov, M. S. Sempere, H. Huang, X. Sun, L. F. Nazar, *Nat. Energy* **2017**, *2*, 17119.

[48] K. Liao, S. Wu, X. Mu, Q. Lu, M. Han, P. He, Z. Shao, H. Zhou, *Adv. Mater*. **2018**, *30*, 1705711.

[49] K. Liu, A. Pei, H. R. Lee, B. Kong, N. Liu, D. Lin, Y. Liu, C. Liu, P.-c. Hsu, Z. Bao, Y. Cui, *J. Am. Chem. Soc*. **2017**, *139*, 4815.

[50] T. Ngoc Duc, D. Lepage, D. Ayme-Perrot, A. Badia, M. Dolle, D. Rochefort, *Angew. Chem. Int. Ed*. **2018**, *57*, 5072.

[51] J. Wang, J. Yang, Q. Xiao, J. Zhang, T. Li, L. Jia, Z. Wang, S. Cheng, L. Li, M. Liu, H. Liu, H. Lin, Y. Zhang, *Adv. Funct. Mater*. **2020**, *31*, 2007434.

[52] C. Yan, X.-B. Cheng, Y.-X. Yao, X. Shen, B.-Q. Li, W.-J. Li, R. Zhang, J.-Q. Huang, H. Li, Q. Zhang, *Adv. Mater*. **2018**, *30*, 1804461.

[53] H. Zhang, X. Liao, Y. Guan, Y. Xiang, M. Li, W. Zhang, X. Zhu, H. Ming, L. Lu, J. Qiu, Y. Huang, G. Cao, Y. Yang, L. Mai, Y. Zhao, H. Zhang, *Nat. Commun.* **2018**, *9*, 3729.

[54] Y. Zhao, G. Li, Y. Gao, D. Wang, Q. Huang, D. Wang, *ACS Energy Lett*. **2019**, *4*, 1271.

[55] C. Fang, J. Li, M. Zhang, Y. Zhang, F. Yang, J. Z. Lee, M.-H. Lee, J. Alvarado, M. A. Schroeder, Y. Yang, B. Lu, N. Williams, M. Ceja, L. Yang, M. Cai, J. Gu, K. Xu, X. Wang, Y. S. Meng, *Nature* **2019**, *572*, 511.

[56] L. Suo, Y.-S. Hu, H. Li, M. Armand, L. Chen, *Nat. Commun*. **2013**, *4*, 1481.

[57] G. Wang, X. Xiong, Z. Lin, J. Zheng, Z. Fenghua, Y. Li, Y. Liu, C. Yang, Y. Tang, M. Liu, *Nanoscale* **2018**, *10*, 10018.

[58] B. Zhu, Y. Jin, X. Hu, Q. Zheng, S. Zhang, Q. Wang, J. Zhu, *Adv. Mater*. **2017**, *29*, 1603755.

[59] J. Chen, Q. Li, T. P. Pollard, X. Fan, O. Borodin, C. Wang, *Mater. Today* **2020**, *39*, 118.

[60] W. Chu, X. Zhang, J. Wang, S. Zhao, S. Liu, H. Yu, *Energy Stor. Mater.* **2019**, *22*, 418.

[61] X. Fan, X. Ji, F. Han, J. Yue, J. Chen, L. Chen, T. Deng, J. Jiang, C. Wang, *Sci. Adv*. **2018**, *4*, eaau9245.

[62] S. Liu, X. Ji, N. Piao, J. Chen, N. Eidson, J. Xu, P. Wang, L. Chen, J. Zhang, T. Deng, S. Hou, T. Jin, H. Wan, J. Li, J. Tu, C. Wang, *Angew. Chem. Int. Ed*. **2021**, *60*, 3661.

[63] Y. Yuan, F. Wu, Y. Bai, Y. Li, G. Chen, Z. Wang, C. Wu, *Energy Stor. Mater*. **2019**, *16*, 411.

[64] Y. Lu, Z. Tu, L. A. Archer, *Nat. Mater.* **2014**, *13*, 961.

[65] X.-B. Cheng, T.-Z. Hou, R. Zhang, H.-J. Peng, C.-Z. Zhao, J.-Q. Huang, Q. Zhang, *Adv. Mater*. **2016**, *28*, 2888.

[66] Q. Liu, D. Zhou, D. Shanmukaraj, P. Li, F. Kang, B. Li, M. Armand, G. Wang, *ACS Energy Lett*. **2020**, *5*, 1456.

[67] A. Pei, G. Zheng, F. Shi, Y. Li, Y. Cui, *Nano Lett*. **2017**, *17*, 1132.

[68] Y. Yu, G. Huang, J.-Z. Wang, K. Li, J.-L. Ma, X.-B. Zhang, *Adv. Mater*. **2020**, *32*, 2004157.

[69] Y. Gao, Z. Yan, J. L. Gray, X. He, D. Wang, T. Chen, Q. Huang, Y. C. Li, H. Wang, S. H. Kim, T. E. Mallouk, D. Wang, *Nat. Mater*. **2019**, *18*, 384.

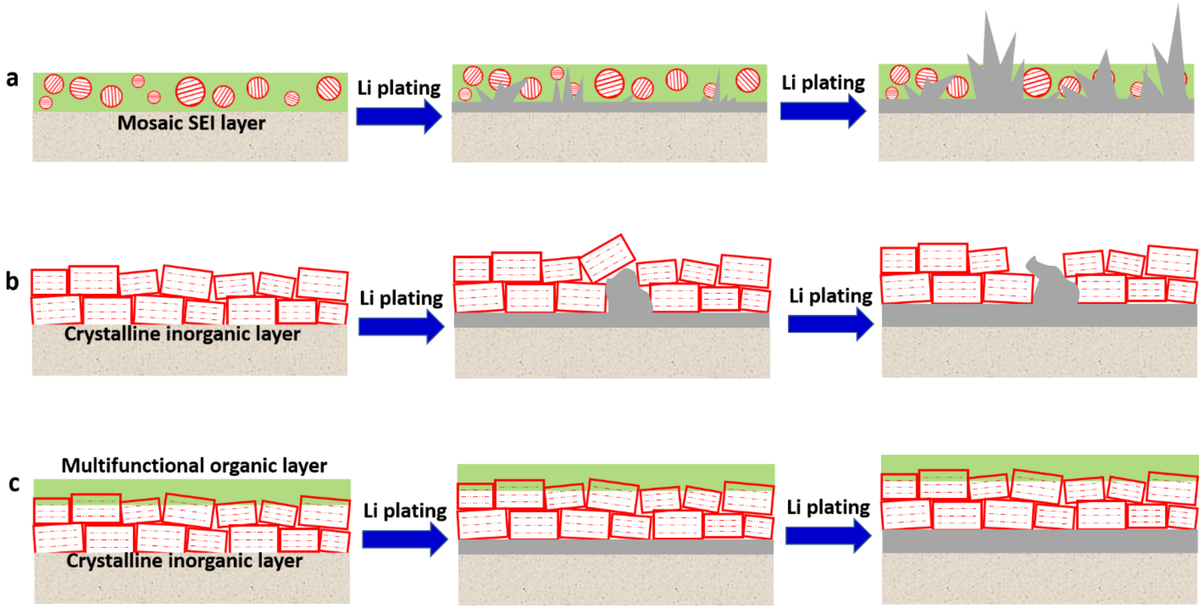

Figure 1. Schematic illustration of various SEI layers for Li plating. a) Mosaic SEI layers. b) Inorganic artificial SEI layers. c) Ordered multifunctional organic/inorganic hybrid SEI layers.

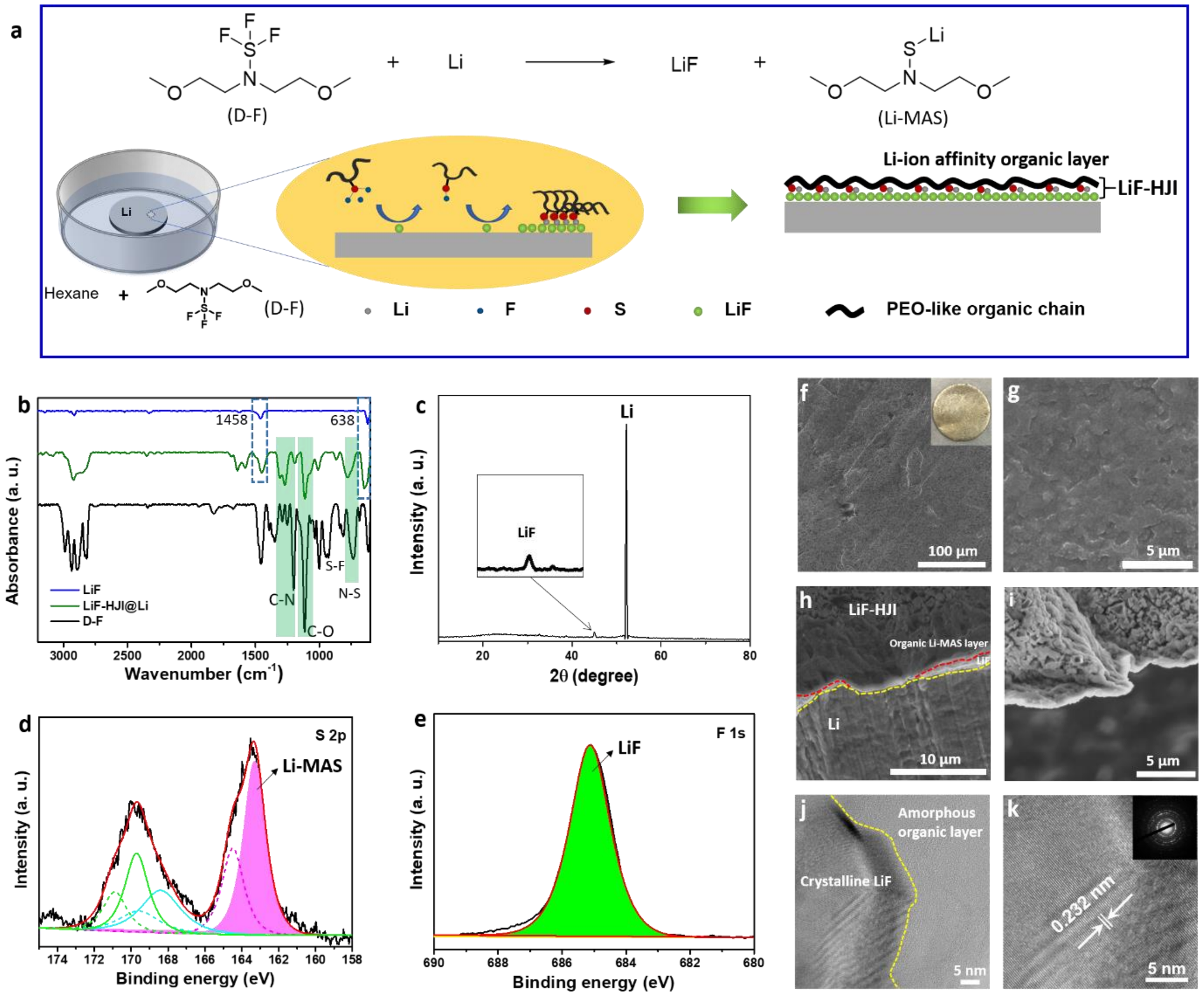

Figure 2. Preparation and characterization of LiF-HJI@Li. a) Schematic illustration of the fabrication of LiF-HJI@Li. b) FT-IR spectra of LiF, LiF-HJI@Li, and D-F. c) XRD pattern of LiF-HJI@Li. d) S 2p XPS spectrum of LiF-HJI@Li. e) F 1s XPS spectrum of LiF-HJI@Li. f, g) Top-view SEM images of LiF-HJI@Li. h, i) Cross-section images of LiF-HJI@Li. j) TEM image of LiF-HJI. k) High-resolution TEM image of LiF-HJI, the inset is the selected area electron diffraction (SEAD) pattern of LiF.

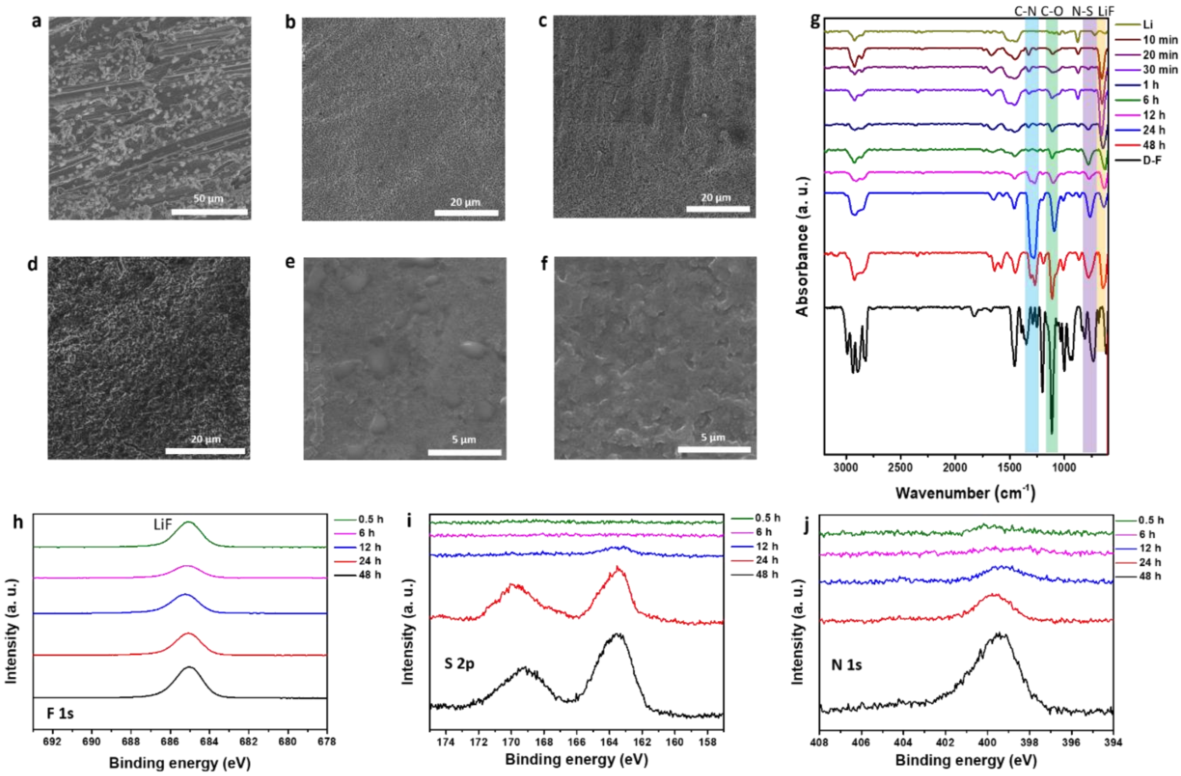

Figure 3. Morphology evolution and corresponding chemical compositions during the formation process of LiF-HJI@Li. SEM morphologies of the Li metal at various soaking times of 10 min (a), 1 h (b), 6 h (c), 12 h (d), 24 h (e), and 48 h (f). (g) FT-IR spectra of the bare Li, treated Li metal after various soaking times, and D-F. F 1s (h), S 2p (i), and N 1s (j) XPS spectra of the Li metal at various soaking times.

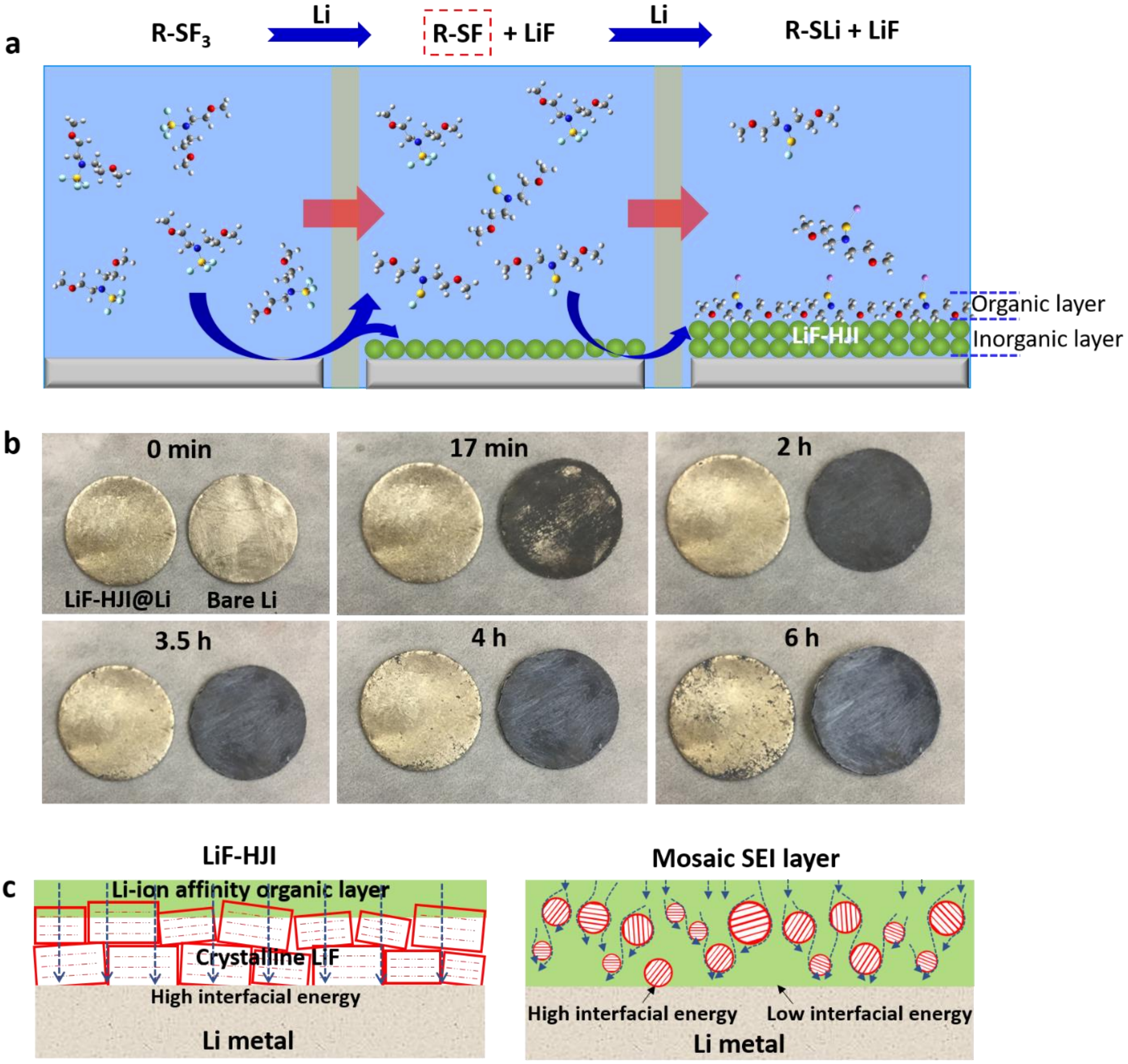

Figure 4. Growth mechanism of LiF-HJI@Li and multifunctional properties of LiF-HJI. a) Growth mechanism of LiF-HJI@Li. b) Stability of LiF-HJI@Li in the humid air (~50% relative humidity). c) Schematic illustration of the different properties between LiF-HJI and traditional mosaic SEI layer. The blue dotted arrows represent the Li-ion transport.

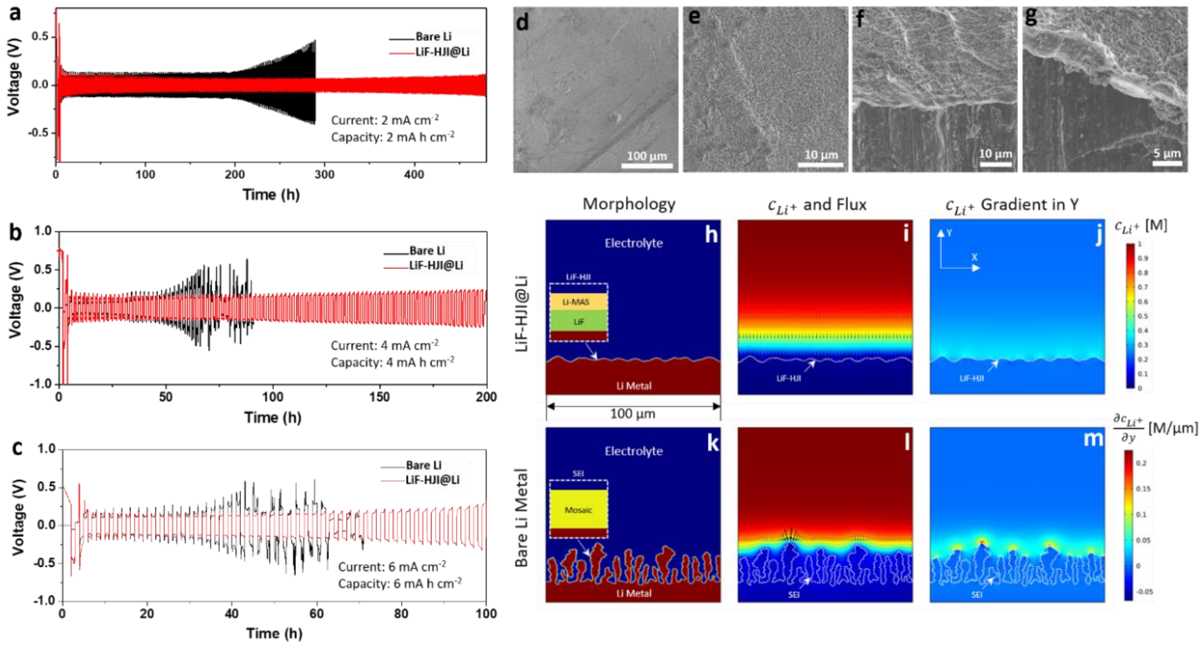

Figure 5. Stability tests of LiF-HJI@Li as electrodes and simulation results of Li deposition under the protection of LiF-HJI. A comparison of the cycling stability of the symmetric LiF-HJI@Li (red) and bare Li metal (black) cells at a current density of 2 mA cm^{-2} (a), 4 mA cm^{-2} (b), and 6 mA cm^{-2} (c)for 1C, respectively. Top-view SEM images (d, e) and cross-section SEM images (f, g) of LiF-HJI@Li after cycling. Simulation results of Li deposition under 2 mA cm^{-2} for 60 min. Simulated Li deposition morphologies of LiF-HJI@Li (h) and bare Li metal (k); simulated Li-ion concentration and flux distribution of LiF-HJI@Li (i) and bare Li metal (l); simulated Li-ion concentration gradient distribution of LiF-HJI@Li (j) and bare Li metal (m). Black arrows in (i) and (l) represent the Li-ion flux.

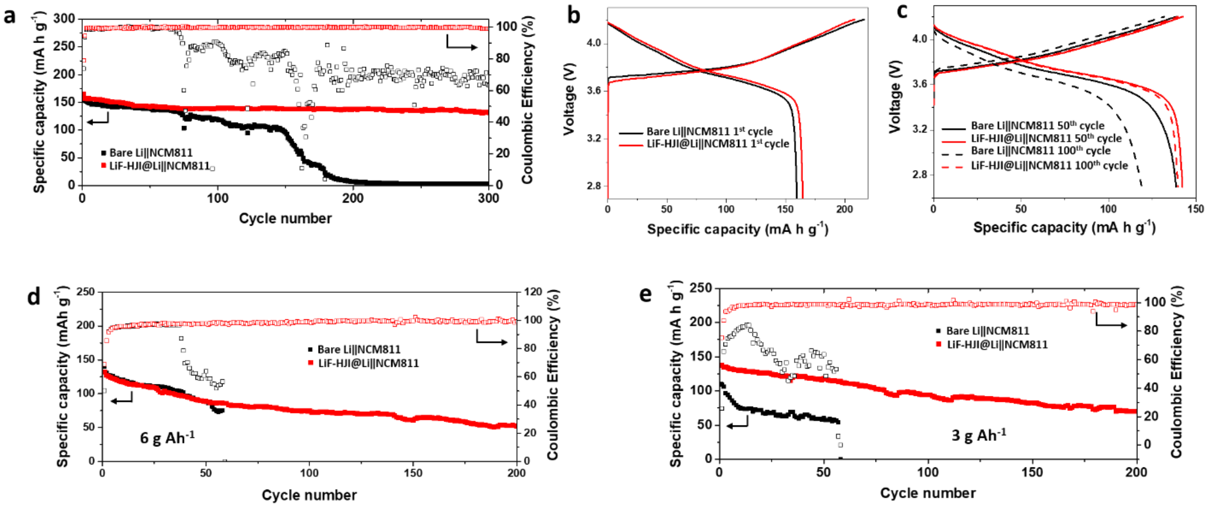

Figure 6. Cycling performance of full cells using LiF-HJI@Li as anodes and NCM811 as cathodes. a) Cycling performance under the flooded-electrolyte condition. b) Charge/discharge profiles during the first cycle. c) Charge/discharge profiles during the 50th and 100th cycles. d) Cycling performance under a lean-electrolyte condition of 6 g Ah^{-1}. e) Cycling performance under a lean-electrolyte condition of 3 g Ah^{-1}. The areal capacity of NCM811 cathode is ~4.2 mA h cm^{-2}.

A controllable design of an ordered LiF-rich organic/inorganic hybrid Janus interphase (LiF-HJI) for high-performance Li metal anodes is reported. LiF-HJI with high SEI/Li interfacial energy and strong Li-ion affinity allows homogenous Li-ion distribution, fast and uniform Li-ion transport, excellent mechanical and passivation properties, enabling stable Li metal anodes under harsh conditions.

Guoxing Li*, Shipeng Liu, Zhe Liu, Yingjie Zhao

High interfacial-energy and lithiophilic Janus interphase enables stable lithium metal anodes